Journal of Colloid and Interface Science 677 (2025) 729–738

Contents lists available at ScienceDirect

Journal of Colloid And Interface Science

journal homepage: www.elsevier.com/locate/jcis

Regular Article

Interfacial electronic modulation of NiCo decorated nano-flowered MoS_2 on carbonized wood as a remarkable bifunctional electrocatalyst for boosting overall water splitting

Mengliang Hu [a,b,1], Yuanpeng Qian [a,1], Rumeng Zhang [c], Chuigen Guo [a], Lemin Yang [a], Liping Li [a,*]

[a] Key Laboratory for Biobased Materials and Energy of Ministry of Education, College of Materials and Energy, South China Agricultural University, 483 Wushan Road, Guangzhou 510642, People's Republic of China
[b] School of Materials, Sun Yat-sen University, Shenzhen 518107, People's Republic of China
[c] School of Environmental Science and Engineering, Sun Yat-Sen University, Guangzhou 510275, People's Republic of China

HIGHLIGHTS

- The NiCo-MoS_2-CW was constructed via hydrothermal and electrodeposition.
- The NiCo-modified MoS_2 significantly enhanced the Volmer step.
- The NiCo-MoS_2-CW can deliver 10 mA cm^{-2} at overpotentials of 64 mV for HER.
- The NiCo-MoS_2-CW || NiCo-MoS_2-CW cell requires only 1.69 V at 50 mA cm^{-2}.

GRAPHICAL ABSTRACT

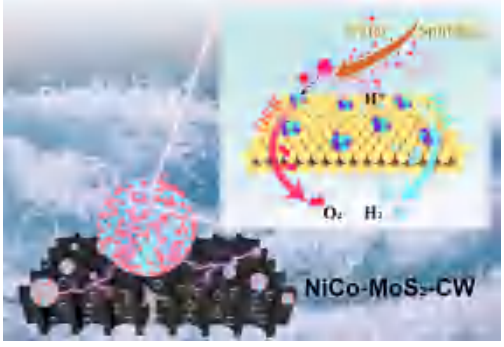

ARTICLE INFO

Keywords:
Carbonized wood electrode
Electrodeposition
MoS_2
Overall Water Splitting

ABSTRACT

The development of a cost-effective and efficient bifunctional electrode for overall water splitting holds significant importance in accelerating the sustainable advancement of hydrogen energy. The present study involved a bifunctional catalytic electrode was prepared by loading NiCo-modified 1T/2H MoS_2 onto carbonized wood (NiCo-MoS_2-CW) using the hydrothermal and electrodeposition techniques. The XPS analysis revealed that NiCo-modified MoS_2 exhibited a weak electron characteristic, which facilitated the ionization of H_2O and significantly enhanced the Volmer step. The XPS analysis unveiled that NiCo-modified MoS_2 displayed a weak electron characteristic, thereby promoting the ionization of H_2O and substantially augmenting the Volmer step. The electrocatalytic performance of the NiCo-MoS_2-CW in 1.0 M KOH is remarkably impressive, exhibiting minimal overpotentials of only 64 mV (10 mA cm^{-2}) and 216 mV (50 mA cm^{-2}) for the hydrogen evolution reaction and oxygen evolution reaction, respectively. The NiCo-MoS_2-CW || NiCo-MoS_2-CW electrolytic cell can achieve a cell voltage of only 1.69 V to achieve a current density of 50 mA cm^{-2}. Overall, this study proposes a potential

* Corresponding author.
E-mail address: lilipingguo@126.com (L. Li).
[1] Mengliang Hu and Yuanpeng Qian contributed equally to this work.

https://doi.org/10.1016/j.jcis.2024.07.209
Received 6 May 2024; Received in revised form 24 July 2024; Accepted 25 July 2024
Available online 26 July 2024

approach to improve the catalytic efficiency of overall water splitting by modulating the interfacial electronic properties of MoS_2.

1. Introduction

Electrolytic water splitting technology holds the potential to efficiently transform unpredictable energy sources (such as wind, solar, tidal, etc.) into environmentally friendly hydrogen energy. This innovation could significantly alleviate challenges like the global energy crisis and environmental pollution [1,2]. The presence of efficient catalysts is essential for accelerating the process of water splitting by facilitating both the hydrogen evolution reaction (HER) and oxygen evolution reaction (OER) [3]. The water splitting process encounters a significant kinetic barrier primarily attributed to the OER during various processes. This reaction process necessitates considerable energy to surmount as it involves a 4 e^- reaction [4]. Currently, Pt-based and Ru/Ir-based materials exhibit superior performance as catalysts for HER and OER. The practical commercial application of noble metal-based catalysts continues to face obstacles such as limited storage and high costs, which impede its accelerated progress [5,6]. In summary, the development and investigation of low noble metal or noble metal-free based bifunctional catalysts for HER and OER are currently of utmost importance.

With the ongoing focus to water splitting technology, many bifunctional electrocatalysts exhibiting exceptional characteristics have been documented, encompassing transition metal sulphides [7–9], nitrides [10–12], selenides [13,14], phosphides [15], etc. The material MoS_2 has attracted considerable attention in the field of HER research due to its two-dimensional nature, extremely low mass density, high surface area-to-volume ratio, and abundant active sites [16]. In particular, the basal surface of the current MoS_2 materials shows limited activity for the catalytic process of HER, while most active sites are primarily concentrated at the edges [17,18]. A feasible approach to overcome these limitations is to optimize the catalytic activity of the substrate through phase transformation engineering [19]. Interestingly, MoS_2 typically exhibits a semiconducting nature in the 1T phase, characterized by edge activity and basal inertness. On the other hand, the 2H phase of MoS_2 is predominantly basal and possesses metallic catalytic activity. However, it is worth noting that the thermodynamic instability of the 1T phase often results in its transformation into the 2H phase, thereby potentially compromising performance stability. Fortunately, recent reports have indicated that the combination of 1T and 2H phases in MoS_2 synthesis plays a crucial role in stabilizing the 1T phase [17]. Additionally, various specialized techniques have been extensively developed to enhance the abundance of active edge sites in MoS_2, including nano-engineering [20], defect engineering [21], single-atom modification [22] and construction of heterojunctions [7]. Among these strategies, nano-engineering is regarded as an optimal approach due to its relatively straightforward methodology and anticipated outcomes. Most typically, it is more advantageous to cultivate MoS_2 nanoflowers/nanosheets directly on a conductive substrate possessing a substantial specific surface area [23]. Therefore, exploring the development and preparation of hybrid phase 1T/2H MoS_2 nanostructures can be deemed as a promising research direction. In terms of catalytic performance for the OER process, MoS_2-based catalysts exhibit limited efficiency, posing a significant challenge to their potential application as bifunctional catalysts in water splitting. Therefore, it is imperative to investigate a strategic approach to enhance the OER activity of MoS_2-based catalysts and fabricate bifunctional catalysts with exceptional performance. The precise modification of MoS_2 is essential to ensure effective catalysis for HER and achieve significant enhancement in catalytic performance for OER. Among numerous modification strategies, such as heteroatom doping [24], structural engineering [25], and coupling with other materials [26], have been shown to be effective in realizing high-performance bifunctional catalysts. The exceptional water splitting properties of the MoS_2 surface can be attributed to the effective combination of dissimilar materials, leading to enhanced charge transfer, improved stability, and modulation of interfacial electrons [2]. Due to its abundant reserves, high cost-effectiveness, and excellent catalytic activity, the modification of MoS_2-based electrocatalysts using Co and Ni as metal components has garnered significant attention [27,28].

On the other hand, the poor electrical conductivity of MoS_2 severely limits the catalytic efficiency [29]. In order to address the aforementioned drawbacks, the current primary approach involves in-situ growth of MoS_2-based materials on a substrate characterized by high specific surface area and excellent electrical conductivity (nickel foam [30], copper foam [31], carbon cloth[32], etc.). Enhancing the conductivity of the material while providing more attachment sites for the active material will significantly enhance the catalytic activity of the electrode material. However, the current application of commercial carbon materials and metal foam materials in the field of overall water splitting has the following disadvantages: (1) The complexity and high cost of the process limit the scale application of carbon-based materials and foam metal; (2) Carbon materials (such as carbon paper and carbon cloth, etc.) lack pore structure along the thickness direction, which limits the mass transfer efficiency; (3) Foam metal is susceptible to corrosion by acidic or alkaline solutions, which significantly reduces the service life of the electrode. In order to compensate for the deficiencies of the conductive matrix, the development of a well-structured, corrosion-resistant, and cost-effective conductive matrix has emerged as a prominent area of research. Among them, carbonized wood (CW), as a conductive substrate with excellent properties, has been widely used in energy storage devices [33–36]. Compared with other conductive substrates, carbonized wood has the following advantages: (1) Compared to foam metal materials, carbonized wood material is resistant to acid and alkali corrosion, which can extend the service life of the electrode; (2) The raw material for CW is wood, a biomass material with abundant reserves; (3) The preparation process of CW is simple and low cost; (4) The CW inherits the porous structure of natural wood, which can not only provide a large number of attachment sites for active substances, but also enhance the mass transfer efficiency. Therefore, considering the aforementioned factors, it is of immense importance to develop a bifunctional electrolytic water electrode by directly incorporating NiCo-modified nano-MoS_2 into CW.

Herein, a highly efficient and durable self-supporting NiCo-modified nano-flowered MoS_2 on CW (NiCo-MoS_2-CW) bifunctional electrode was constructed via hydrothermal and electrodeposition strategy for HER and OER. Interestingly, the MoS_2 nanosheets in the electrode exhibited a unique hybrid phase of 1T/2H, forming nanoflowers that fully exposed the edge active sites while leaving the basal surface uncovered. Meanwhile, NiCo modification of MoS_2 increased the number of active sites, which was fully verified by C_{dl} values. In particular, the XPS analysis revealed the impact of NiCo-modified MoS_2 on the electronic structure of the surface, while the Tafel value provided further evidence of its influence on the Volmer process. As a result of promoting the Volmer process, complete exposure of active sites, and increased active site density, the NiCo-MoS_2-CW electrode demonstrated exceptional performance in both HER and OER. As expected, the NiCo-MoS_2-CW can deliver 10 mA cm^{-2} at overpotentials of 64 mV for HER and 50 mA cm^{-2} at overpotentials of 331 mV for OER. Impressively, NiCo-MoS_2-CW as both cathode and anode only a voltage of 1.69 V is required to drive a current density of 50 mA cm^{-2}. This research presents promising opportunities for utilizing MoS_2-based catalysts in electrocatalytic overall water splitting applications.

2. Experimental section

2.1. Materials

Sodium molybdate dehydrate ($Na_2MoO_4·2H_2O$, 99 %), nickel chloride ($NiCl_2$, 98 %) and cobaltous chloride ($CoCl_2$, 98 %) were provided from SAAN Chemical Technology Co., Ltd. (Shanghai, China). Thiourea (CH_4N_2S, 98 %) was purchased from Adamas-beta®. (Shanghai, China). Ethanol (CH_3CH_2OH, 99.5 %) was provided from Bei Jing TongGuang Fine Chemicals Company (Beijing, China). Nitric acid (HNO_3, 65 ~ 68 %) was provided by Guangshi reagent Technology Co., Ltd. (Guangdong, China). Acetone (CH_3COCH_3, 99.5 %) was acquired from ANPEL Scientific Instrument Co., Ltd (Shanghai, China). Pt/C (20 wt%) and RuO_2 (99.95 %) were provided from Shanghai Macklin Biochemical Co., Ltd. in China. Nafion solution (5 %) was purchased from Du Pont Company. The above reagents are analytically pure and have not been further purified.

2.2. Synthesis of MoS_2-CW

The CW was prepared and preprocessed according to our previous report [32]. Briefly, carbonized wood is prepared by oxygen-free calcination in a tube furnace (BTF-1400C, Anhui BEQ Equipment Technology Co., Ltd., China). To synthesize MoS_2-CW, 0.125 mol $Na_2MoO_4·2H_2O$ and 1 mol CH_4N_2S were dissolved in 50 mL distilled water form mixed solution and poured into the reagent bottle (PakGent®) for use. The solution and CW were introduced into Teflon-lined stainless steel autoclave lined with polytetrafluoroethylene at 190 °C for 15 h. Subsequently, electrode washing with deionized water and ethanol, respectively, and dried under vacuum at 50 °C for 24 h, was recorded as MoS_2-CW.

2.3. Synthesis of NiCo-MoS_2-CW

NiCo-MoS_2-CW electrode was prepared via electrodeposition method, 0.002 mol $NiCl_2$, 0.001 mol $CoCl_2$, 0.025 mol H_3BO_3, and 0.025 mol NH_4Cl were dissolved in 50 mL distilled water form homogeneous solution. Briefly, the electrodeposition process was carried out in a three-electrode system, using MoS_2-CW electrode, graphite rod and saturated calomel electrode as the working electrode, the counter electrode and the reference electrode, respectively. Three CV cycles were carried out in the potential window of -0.2 ~ -1.5 V (vs. SCE) at a scanning speed of 25 mV/s, was recorded as NiCo-MoS_2-CW. In addition, NiCo-CW was obtained by electrodeposition directly on CW.

2.4. Materials characterization

Scanning electron microscopy (SEM) combined with Energy-dispersive X-ray (EDX) images were investigated on a ZEISS EVO18. Field-emission scanning electron microscopic (FE-SEM) and was recorded with Hitachi SU8220. High resolution transmission electron images (TEM) equipped with EDX were used to characterize the morphology. X-ray diffraction (XRD, Ultima IV Rigaku) studies the crystal structure of the material. X-ray photoelectron spectra (XPS) were analyzed by Thermo Scientific K-Alpha X-ray photoelectron spectrometer.

2.5. Electrochemical measurements

All electrochemical measurements were performed utilizing a three-electrode cell in 1.0 M KOH solution, employing an electrochemical workstation (CHI660E, Chenhua, China). Among them, the as-prepared electrodes, graphite rod and saturated calomel electrode (SCE) are used as working electrode, counter electrode and reference electrode respectively. For comparison, Pt/C and RuO_2 of the same mass are loaded on CW respectively. All potentials measured were calibrated to the reversible hydrogen electrode (RHE) using the Nernst equation: $E_{RHE}=E_{SCE}+0.244\ V+0.059\ pH$ (1.0 M KOH, pH=14). The electrocatalytic activity of the electrodes was evaluated using linear sweep voltammetry (LSV) with a scan rate of 1 mV/s and iR-correction. Meanwhile, the Tafel plot was subsequently derived from the equation: $\eta = b \log j + a$, where η (V) is the overpotential, j (mA cm^{-2}) is the current density, b (V dec^{-1}) is the Tafel plot. Overall water splitting evaluation was conducted in a cell utilizing the NiCo-MoS_2-CW as both the anodic and the cathodic electrodes. Electrochemical impedance spectroscopy (EIS) measurements were carried out by applying AC voltage of 5 mV within a frequency range from 10^{-2} to 10^5 Hz. Furthermore, an electrochemically active surface area (ECSA) was derived from the double-layer capacitance (C_{dl}). The stability test of the NiCo-MoS_2-CW electrode was conducted at the overpotential of -65 mV (HER), 150 mV (OER) and 1.5 V (overall water splitting) for 24 h.

The mass activity (MA) was evaluated by the following equation: $MA=i/m$, where i represents the measured current, m is the mass of electrode.

3. Results and discussion

3.1. Synthesis and characterization of NiCo-MoS_2-CW electrode

Fig. 1a shows the synthesis illustration of NiCo-MoS_2-CW electrodes. For comparison, the optical photos of CW, NiCo-CW, MoS_2-CW, and NiCo-MoS_2-CW electrodes are presented in Figure S1 (Supporting Information), where the observed color changes provide initial confirmation of the successful synthesis of these electrodes. The quality of the CW, MoS_2-CW, NiCo-CW, and NiCo-MoS_2-CW electrodes is illustrated in Figure S2. Initially, a hydrothermal method was employed to incorporate nanoflower-like MoS_2 onto the CW substrate. As depicted in Fig. 1b_1-b_3, the SEM images presented demonstrate the smooth morphology of the CW surface after undergoing pre-treatment. After the hydrothermal reaction, Fig. 1c_1-c_3 shows the nanoflower-like MoS_2 structure on the CW surface. Interestingly, the nanoflower-like structure formed by uniformly stacking sheet MoS_2 is clearly depicted in Fig. 1c_3. The full catalytic potential can be fully realized by ensuring an equal distribution of active sites on the outer surface while keeping the base surface free from coverage. Finally, the NiCo-MoS_2-CW electrode is obtained through the in-situ electrodeposition of NiCo onto MoS_2-CW. As shown in Fig. 1d_1-d_2, after NiCo is modified on the surface of MoS_2, MoS_2 on the electrode surface can still maintain a nanoflower-like structure, which is the key to maintain the intrinsic activity of MoS_2. However, SEM images (Fig. 1d_3) with high magnification showed that NiCo of MoS_2 surface load was clearly visible, which also indicated further improvement of catalytic performance. Meanwhile, Figure S3a-b (Supporting Information) shows the SEM image of NiCo-CW electrode. Compared to Fig. 1b_1-b_3, it is apparent that the CW surface displays a noticeable presence of NiCo. The absence of distinct nanostructures, however, suggests potential constraints on its electrocatalytic performance. The SEM image and corresponding energy dispersive X-ray (EDX) elemental mapping images of MoS_2-CW and NiCo-MoS_2-CW are depicted in Fig. 1e_1-e_5 and Fig. 1f_1-f_5, respectively. Among them, the surface of the MoS_2-CW electrode exhibits the presence of S and Mo elements, indicating the existence of a nanoflower structure composed of MoS_2. Additionally, uniform distribution of Ni, Co, S and Mo elements is observed on the surface of the NiCo-MoS_2-CW electrode, providing evidence for successful modification with NiCo onto the MoS_2-CW electrode. In addition, the EDX spectrum indicates that the main components of the NiCo-MoS_2-CW and MoS_2-CW electrode primarily consists of C (46.58 at.% and 57.87 at.%), S (21.87 at.% and 28.35 at.%), Mo (10.21 at.% and 13.81 at.%), Co (10.81 at.%) and Ni (10.53 at.%) elements, as depicted in Table S1 and Table S2 (Supporting Information). In summary, SEM images of electrodes confirm that NiCo modified nanoflower-like MoS_2 is successfully loaded on CW.

The X-ray diffraction (XRD) patterns of as-prepared NiCo-MoS_2-CW, NiCo-CW, MoS_2-CW and CW are depicted in Fig. 2a. For the NiCo-CW,

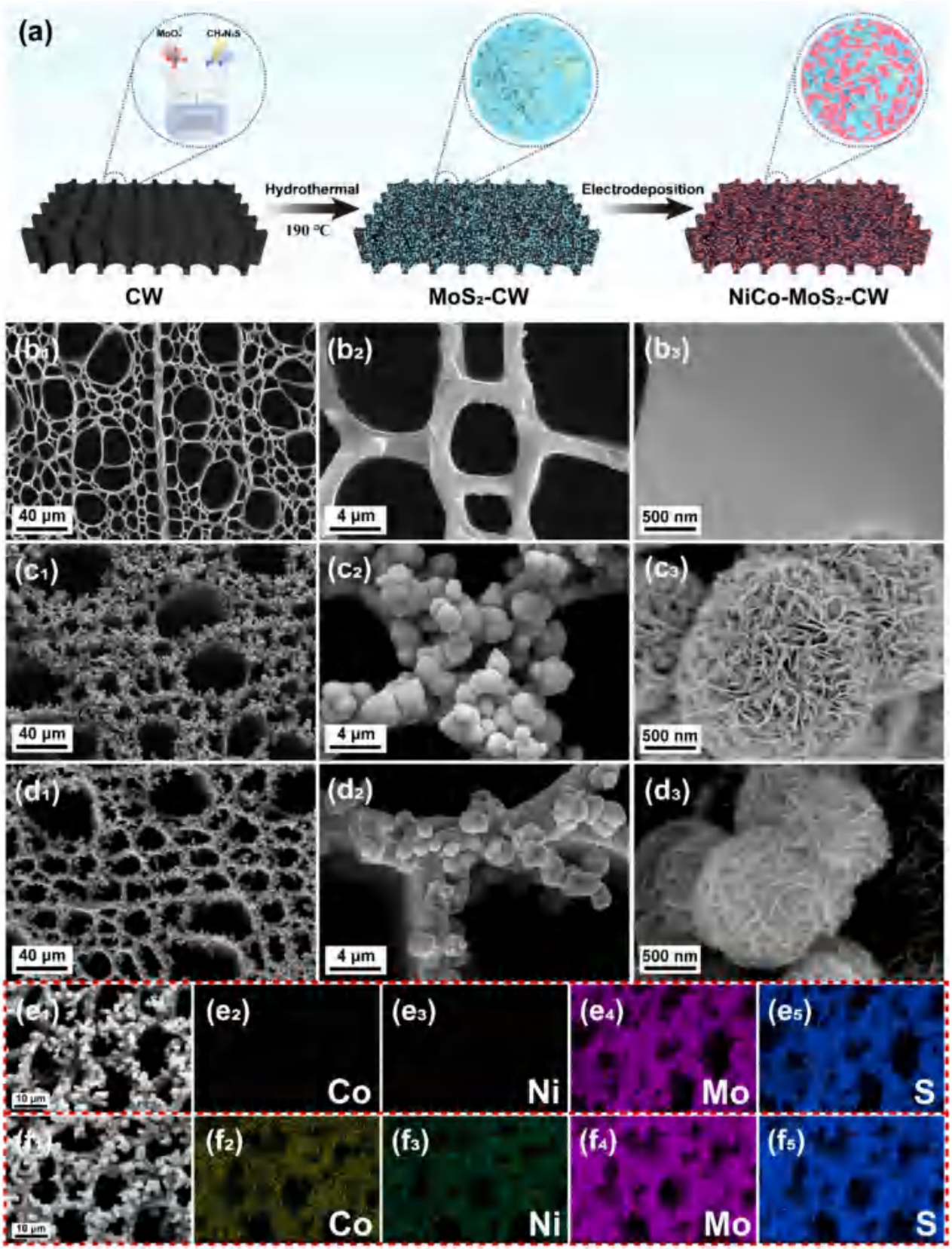

Fig. 1. a) Schematic illustration for the preparation of NiCo-MoS_2-CW electrodes; SEM images of b_1-b_3) CW, c_1-c_3) MoS_2-CW, d_1-d_3) NiCo-MoS_2-CW; SEM-EDS mapping images of e_1-e_5) MoS_2-CW and f_1-f_5) NiCo-MoS_2-CW for different elements.

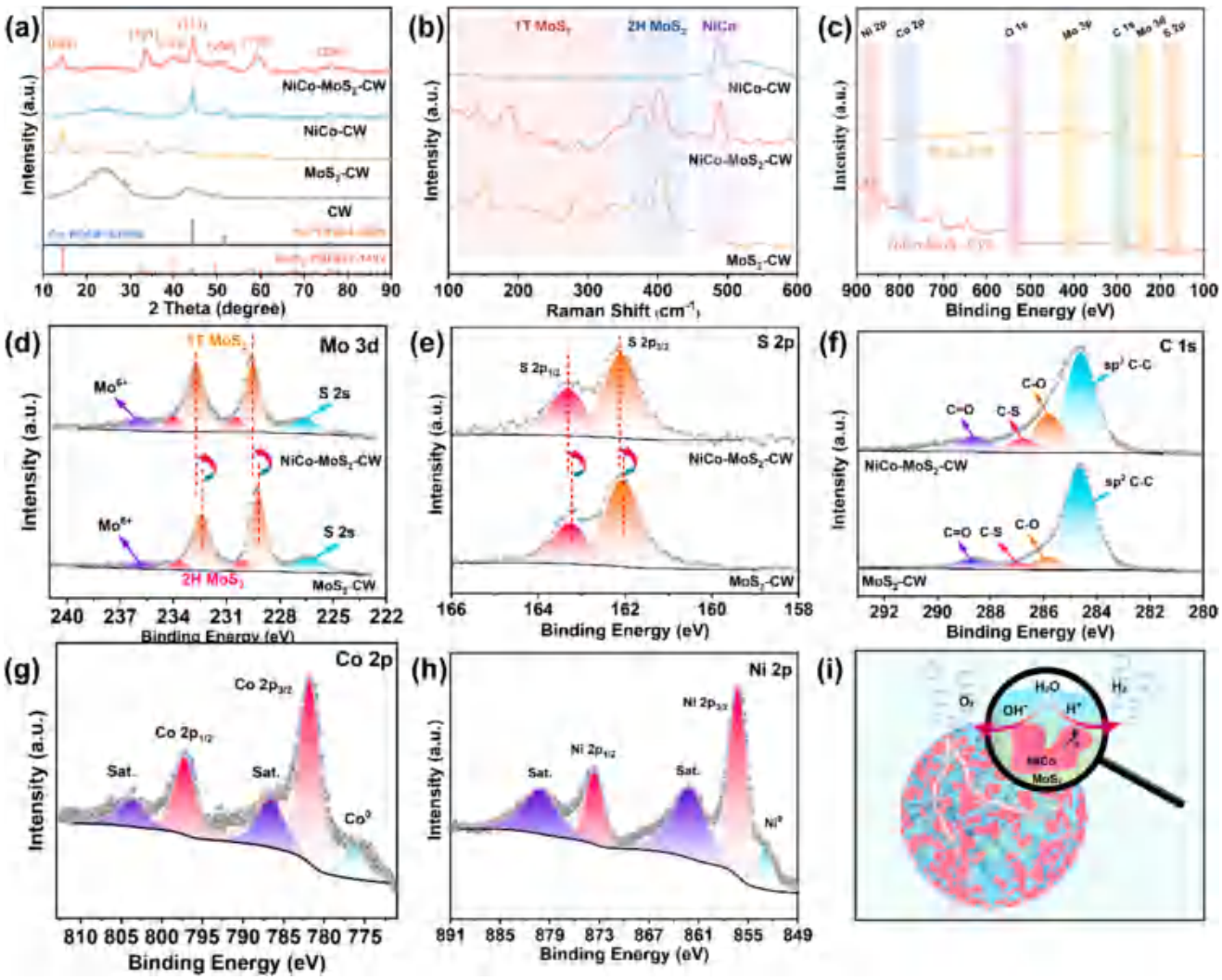

Fig. 2. a) XRD patterns of CW, NiCo-CW, MoS_2-CW and NiCo-MoS_2-CW; b) Raman spectra of NiCo-CW, MoS_2-CW and NiCo-MoS_2-CW; c) XPS survey spectra, d) Mo 3d, e) S 2p and f) C 1 s spectra of MoS_2-CW and NiCo-MoS_2-CW; g) Co 2p and h) Ni 2p spectra of NiCo-MoS_2-CW; i) The structure models of NiCo-MoS_2-CW and the schematic illustration of the efficient overall water splitting on NiCo-MoS_2-CW.

the diffraction peaks at 44.5°, 51.8° and 76.4° can be assigned to (1 1 1), (2 0 0), and (2 2 0) planes of NiCo (PDF#04–0850)[37,38], respectively, whereas those at 14.4°, 33.5°, 39.5°, and 58.3° can be indexed to (0 0 2), (1 0 1), (1 0 3) and (1 1 0) reflection planes of MoS_2 (PDF#37–1492), respectively. As expected, the XRD plot of NiCo-MoS_2-CW exhibits distinct diffraction peaks corresponding to NiCo and MoS_2, providing further confirmation of the successful modification of NiCo onto MoS_2. For CW, the two wider characteristic diffraction peaks correspond to the (0 0 2) and (1 0 0) crystal faces of carbon. In the Raman spectrum (Fig. 2b), the characteristic vibration peaks at 146 cm^{-1} (J_1), 235 cm^{-1} (J_2), 281.5 cm^{-1} (E_g) and 335 cm^{-1} (J_3) are attributed to 1 T MoS_2[18]. In addition, the fingerprint peaks of 378 cm^{-1} and 403 cm^{-1} confirm the existence of 2H MoS_2. Hence, the outcomes obtained provide evidence that the nanoflower-shaped MoS_2 exhibits dual phases consisting of 1T and 2H. In particular, a characteristic peak appears at 472 cm^{-1} in NiCo-CW, indicating that the metal may be oxidized. The Raman spectra acquired from NiCo-MoS_2-CW displayed the same distinctive peaks observed in both NiCo-CW and MoS_2-CW, thus offering additional confirmation of the successful integration of NiCo-modified MoS_2 onto CW.

The survey spectra confirm the presence of S 2 s, Mo 3p and S 3d signals in both MoS_2-CW and NiCo-MoS_2-CW electrodes (Fig. 2c). In particular, the survey spectrum of NiCo-MoS_2-CW exhibits characteristic peaks of Ni 2p and Co 2p, distinguishing it from MoS_2-CW and indicating the successful incorporation of NiCo-modified MoS_2 onto CW. In Fig. 2d, for MoS_2-CW, Mo^{4+} 3d peaks of 1 T MoS_2 are shown at 229.3 eV and 232.4 eV. In addition, the Mo 3d spectrum displays peaks at 230.7 eV and 234.0 eV which can be associated with the presence of Mo^{4+} 3d orbitals in the 2H MoS_2 structure, while a binding energy of 235.9 eV is indicative of the presence of Mo^{6+}. Interestingly, in comparison to the Mo^{4+} 3d peaks observed in the MoS_2-CW electrode, a positive shift was observed for the NiCo-MoS_2-CW, indicating that the introduction of NiCo modifies the electronic properties of the NiCo-MoS_2-CW surface. In Fig. 2e, for MoS_2-CW, the peak at 162.1 eV and 163.3 eV can be ascribed to the characteristic peak of S $2p_{1/2}$ and $2p_{3/2}$. Similar to Mo 3d, the S 2 s characteristic spectra of NiCo-MoS_2-CW electrodes all showed positive shifts, which again confirmed the weak electronic characteristics on the surface of NiCo-MoS_2-CW after NiCo modification. Consequently, the relatively weak electron characteristics of the surface will enhance the absorption of OH^- at the interface and accelerate the kinetic progression of OER. For C 1 s (Fig. 2f), the main characteristic peaks at 284.6 eV, 285.8 eV, 286.8 eV and 288.6 eV, indicative to the sp^2 C—C, C—O, C—S and C═O bond, respectively. Displayed in Fig. 2g, Co exists mainly as Co metal with a 2p3/2 peak at 781.8 eV. Similarly, Ni 2p XPS spectrum exhibits a main board peak centered at 856.2 eV corresponds to the signal of Ni metal [36]. The introduction of NiCo modification is

anticipated to enhance the ionization of H_2O, as illustrated in Fig. 2i. Consequently, this enhancement will facilitate both HER and OER processes by improving its electronic properties.

The transmission electron microscopy (TEM) images were utilized to conduct a detailed analysis of the structure and morphology of NiCo-MoS_2. The TEM image of NiCo-MoS_2 in Fig. 3a reveals distinct contrasts corresponding to various nanoflake MoS_2 structures, which is consistent with the observations from SEM imaging. Furthermore, a high-resolution TEM image (Fig. 3b) reveals the edge position of the NiCo-MoS_2 nanoflower, displaying lattice fringes with a facial spacing measuring 0.62 nm that corresponds to the (002) crystal face of MoS_2. In the HRTEM image that has been further magnified (Fig. 3c), both the 1 T phase (pink region) and the 2H phase (yellow region) are observed on a single MoS_2, which is in agreement with the findings from Raman spectroscopy. The distinct contrast between the 1 T phase and the 2H phase depicted in the figure corresponds to a top-down view of their respective three-dimensional structural models as shown in Fig. 3c_1 and 3c_2. The HRTEM image (Fig. 3d) demonstrates the presence of lattice fringes with interplanar spacing measuring 0.62 nm and 0.22 nm, which correspond to the crystal plane of MoS_2 (002) and NiCo (111). The simultaneous observation of the selected area electron diffraction (SAED) pattern for NiCo-MoS_2-CW provides unequivocal confirmation of the structure's high crystallinity through the detection of a distinct diffraction ring. In addition, the FFT inverse patterns in Fig. 3d_1 and d_3 correspond to area 1 and 2 in Fig. 3c. Meanwhile, as shown in Fig. 3d_2 and 3d_4, the intensity curves of the lattice in the red region of Fig. 3d_1 and 3d_3 confirm that the plane spacing of 0.62 nm and 0.22 nm corresponds to the MoS_2 (002) plane and NiCo (111) plane. In addition, the high-angle annular dark-field scanning transmission electron microscopy (HAADF-STEM) and corresponding element mapping images reveal a homogeneous distribution of Ni, Co, C, Mo, and S elements (Fig. 3e-k). The aforementioned analysis demonstrates the successful loading of NiCo-modified nanoflower-like MoS_2 with a mixed-phase composition of 1T and 2H onto CW. These findings align with the results obtained from XRD, XPS, and Raman spectrograph analyses.

3.2. HER performance of NiCo-MoS_2-CW electrode

To assess the electrocatalytic efficiency, the electrodes were subjected to HER testing in a solution containing 1.0 M KOH. As depicted in Fig. 4a-4b and Figure S4, the overpotentials observed for NiCo-MoS_2-CW at 10 mA cm^{-2}, 100 mA cm^{-2} and 200 mA cm^{-2} are measured to be 64 mV, 182 mV and 233 mV, respectively, which are superior to those of MoS_2-CW (104 mV, 267 mV and 360 mV) and NiCo-CW (127 mV, 376 mV and 510 mV). The catalytic performance of the NiCo-MoS_2-CW electrode is significantly enhanced as a result of incorporating NiCo into MoS_2. In addition, as shown in Figure S5, the MA of NiCo-MoS_2-CW electrode is better than CW, NiCo-CW and NiCo-MoS_2-CW. Accordingly, Fig. 4c depicts the Tafel slope diagram derived from transforming LSV curves of various electrodes, which is used to evaluate HER kinetic

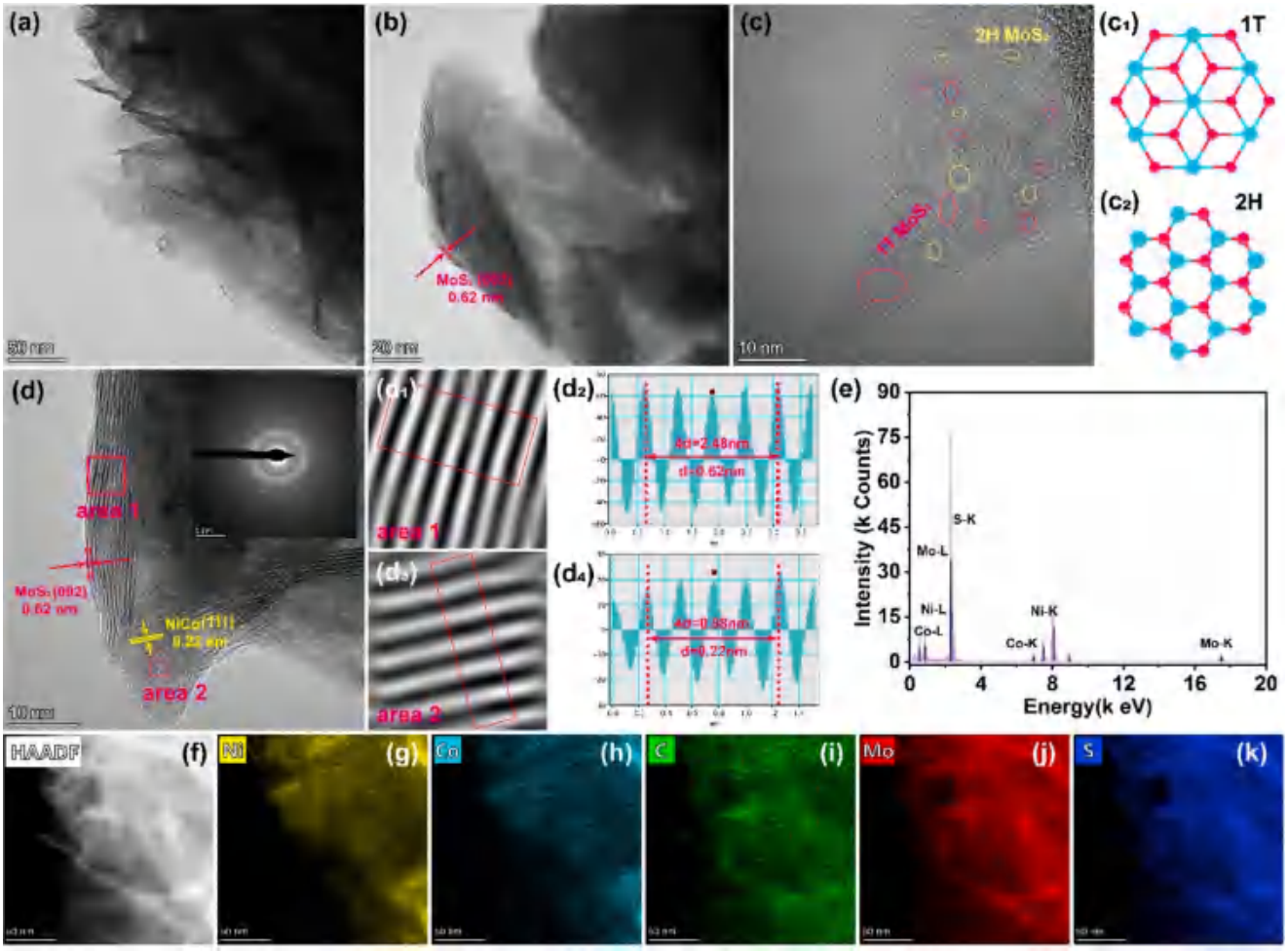

Fig. 3. a) TEM images; b)- c) HRTEM images of NiCo-MoS_2-CW, top view of c_1) 1T MoS_2 and c_2) 2H MoS_2; d) High-magnification HRTEM image of NiCo-MoS_2-CW and the SAED pattern, corresponding inverse FFT patterns of d_1) area 1 and d_3) area 2, intensity profiles d_2) and d_4) for the red area of d_1) and d_3); e) The EDX microanalysis of the as-synthesized NiCo-MoS_2-CW electrode for f)- k) STEM images; f) HAADF-STEM images and g)- k) related elemental mapping images of the NiCo-MoS_2-CW. (For interpretation of the references to color in this figure legend, the reader is referred to the web version of this article.)

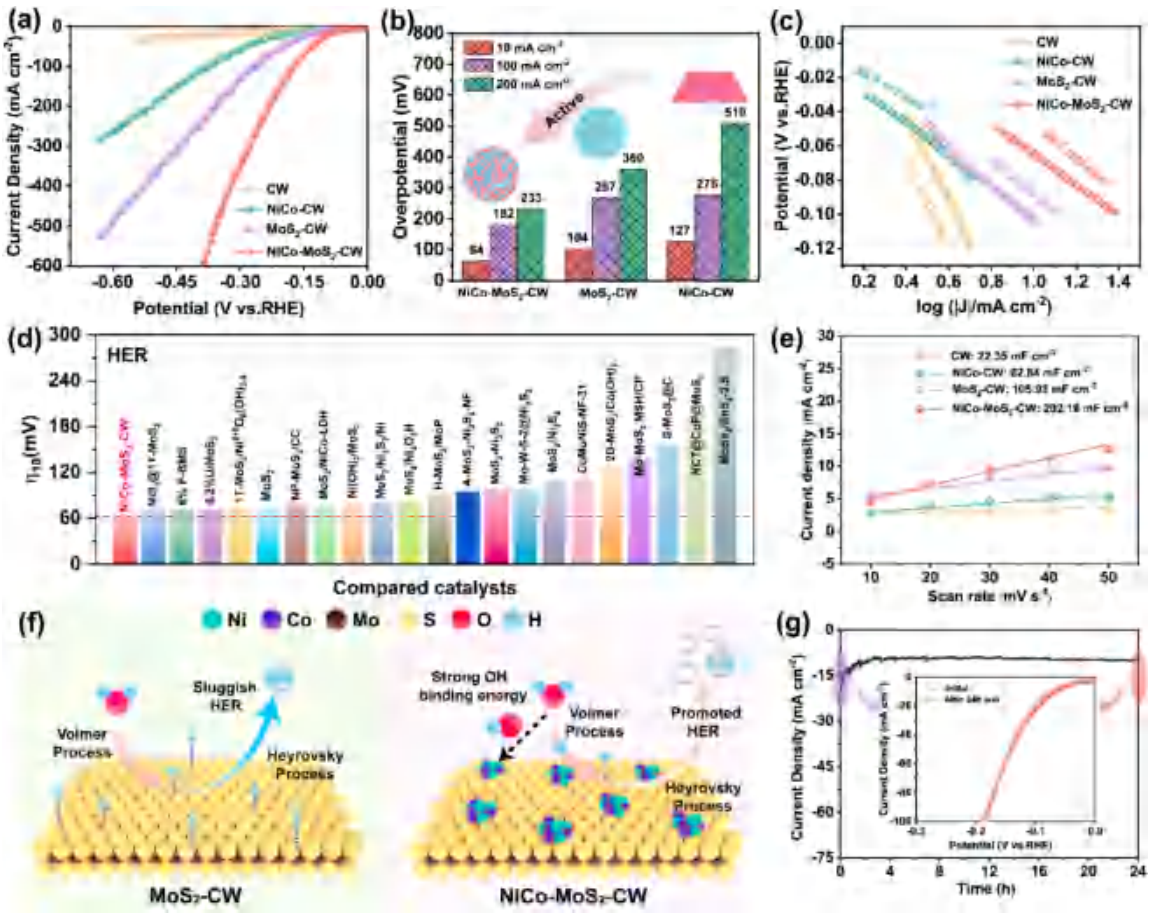

Fig. 4. HER performance of synthesized catalysts in 1.0 M KOH, a) the linear sweep voltammetry (LSV) curves of the CW, NiCo-CW, MoS_2-CW and NiCo-MoS_2-CW; b) comparison of HER overpotentials at 10 mA cm^{-2}, 100 mA cm^{-2} and 200 mA cm^{-2} for NiCo-CW, MoS_2-CW and NiCo-MoS_2-CW; c) Tafel slopes of the CW, NiCo-CW, MoS_2-CW and NiCo-MoS_2-CW; d) comparison of the HER performance of NiCo-MoS_2-CW with reported MoS_2-based catalysts at a current density of −10 mA cm^{-2}, originating from Table S3 (Supporting Information); e) Double-layer capacitance (C_{dl}) for the CW, NiCo-CW, MoS_2-CW and NiCo-MoS_2-CW; f) schematic illustration of Volmer process and Heyrovsky process: MoS_2-CW and NiCo-MoS_2-CW; g) the chronoamperometry curve of NiCo-MoS_2-CW at the overpotential −64 mV, the inset shows LSV curves before and after 24 h.

process. The Tafel slope value observed for the NiCo-MoS_2-CW electrode is 89.5 mV dec^{-1}, indicating that the catalytic process of HER is governed by the Volmer–Heyrovsky mechanism. However, it is worth noting that the Tafel slope values obtained for NiCo-MoS_2-CW electrodes demonstrate a significant decrease in comparison to those of CW, NiCo-CW, and MoS_2-CW electrodes. This observation implies a remarkable enhancement in the Heyrovsky process following the modification with NiCo. To assess performance at 10 mA cm^{-2} overpotentials, we compared the overpotential of the NiCo-MoS_2-CW electrode with that reported previously for MoS_2-based catalysts (Fig. 4d and Table S3, Supporting Information) [2,39–58]. After conducting a comprehensive analysis, it becomes evident that the NiCo-MoS_2-CW electrode outperforms most MoS_2-based electrodes, thereby emphasizing the exceptional advantages of utilizing the NiCo-MoS_2-CW electrode to enhance the HER process.

Furthermore, the EIS measurement results (Figure S6, Supporting Information) demonstrate that the NiCo-MoS_2-CW electrode exhibits a considerably reduced charge transfer resistance compared to other electrodes. The incorporation of NiCo into MoS_2 effectively enhances the rate of charge transfer during the process of HER, indicating a significant improvement in catalytic activity. As shown in Fig. 4e, the electrochemical double layer capacitor (C_{dl}) is utilized to assess the catalytic efficiency of the electrode by reflecting its electrochemically active surface area. The determination of C_{dl} value for the electrode was carried out using cyclic voltammetry at different scanning rates within a non-Faraday potential range (Figures S7a-4d, Supporting Information). Excitingly, the C_{dl} of the NiCo-MoS_2-CW electrode is 201.6 mF cm^{-2}, which is 1.9 ~ 9 times that of the CW (22.35 mF cm^{-2}), NiCo-CW (62.84 mF cm^{-2}) and MoS_2-CW (105.93 mF cm^{-2}) electrodes. Based on the results obtained from SEM and XPS analysis, it can be inferred that the incorporation of NiCo into MoS_2 leads to a substantial enhancement in the electrochemically active surface area.

This enhancement is primarily attributed to an augmentation in the number of active sites resulting from the modification of MoS_2 with NiCo. As indicated by the outcomes of XPS analysis, there is evidence suggesting that the electron characteristics on the surface of NiCo-MoS_2-CW electrode are relatively weak. The schematic diagram (Fig. 4f) illustrates that the NiCo-MoS_2-CW electrode surface possesses a strong affinity towards OH^- owing to its weak electronic characteristics. It can be predicted that the strong adsorption of OH^- on the electrode surface will obviously promote the whole oxygen evolution reaction process, which will lead to a significant improvement of electrocatalytic oxygen evolution performance. On the other hand, the strong adsorption of OH^- on the electrode surface will promote the ionization process of H_2O. Inevitably, the rapid ionization of H_2O will accelerate the adsorption process of H^+ on the surface. The Tafel slope results in Fig. 4c show that the Volmer process of the NiCo-MoS_2-CW electrode is promoted, thus speeding up the overall catalytic process. Long-term stability, as an important criterion to evaluate the practicability of electrodes, has been concerned. The stability test in Fig. 4g was conducted continuously for

24 h at an overpotential of −64 mV (vs. RHE). Remarkably, the electrode NiCo-MoS_2-CW exhibits consistent current density throughout the test, indicating its impressive durability. Additionally, Fig. 4g illustrates a strong correlation between the LSV curves prior to and following the stability test, providing further substantiation of the exceptional stability exhibited by NiCo-MoS_2-CW. In addition, compared with before the stability test, the SEM image of the electrode surface did not change after the test (Figure S8, Supporting Information), indicating that the microstructure of the electrode also has good durability. At the same time, it was observed that the XPS analysis results remained unchanged after conducting the stability test (Figure S9, Supporting Information). The enduring nature of the NiCo-MoS_2-CW electrode composition is further substantiated. Consequently, these aforementioned experiments provide substantial evidence to support the exceptional hydrogen evolution reaction (HER) performance exhibited by the NiCo-MoS_2-CW electrode.

3.3. OER performance of NiCo-MoS_2-CW electrode

The OER performance of all samples were tested in 1.0 M KOH electrolyte. As shown in Fig. 5a and Figure S10, the NiCo-MoS_2-CW electrode (pink curve) showed the best catalytic activity for OER in all samples. The overpotential of the electrodes fabricated in this investigation at different current densities is depicted in Fig. 5b. The NiCo-MoS_2-CW electrode requires only 331 mV, 370 mV, and 420 mV to achieve current densities of 50,100, and 200 mA cm^{-2}, respectively, which is significantly lower than NiCo-CW and MoS_2-CW. In addition, as shown in Figure S5, the MA of NiCo-MoS_2-CW electrode is better than CW, NiCo-CW and NiCo-MoS_2-CW. The Tafel slope of the electrodes prepared in this study at various current densities is illustrated in Fig. 5c. The Tafel slope of NiCo-MoS_2-CW (116.3 mV dec^{-1}) was significantly lower than that of MoS_2-CW (272.6 mV dec^{-1}), NiCo-CW (187.2 mV dec^{-1}) and CW (455.0 mV dec^{-1}). In particular, MoS_2-CW and NiCo-CW electrodes larger than 120 mV dec^{-1} indicate that the catalytic process is predominantly governed by the Volmer mechanism. As illustrated in Fig. 4f, the schematic representation of Volmer process and Heyrovsky process reveals that the presence of NiCo modification induces a modification in the electronic configuration of the MoS_2 surface. The modification increases the surface's affinity for adsorbing OH^-, thereby effectively promoting the Volmer process. Hence, the Tafel slope observed in the NiCo-MoS_2-CW electrode (116.3 mV dec^{-1}) indicates that the catalytic process is primarily influenced by the Volmer–Heyrovsky mechanism, thus providing further support to the XPS findings. Notably, the OER performance of the NiCo-MoS_2-CW electrode was compared to other MoS_2-based electrodes (Fig. 5d and Table S4, Supporting Information) [59–73]. The exciting finding is that the overpotential needed for the NiCo-MoS_2-CW electrode to achieve a current density of 50 mA cm^{-2} surpasses that required by other electrodes to reach only 10 mA cm^{-2}. Based on the EIS findings depicted in Fig. 5e, it is apparent that the NiCo-MoS_2-CW electrode demonstrates superior charge transfer resistance when compared to CW, NiCo-CW, and MoS_2-CW electrodes. The results indicate a substantial

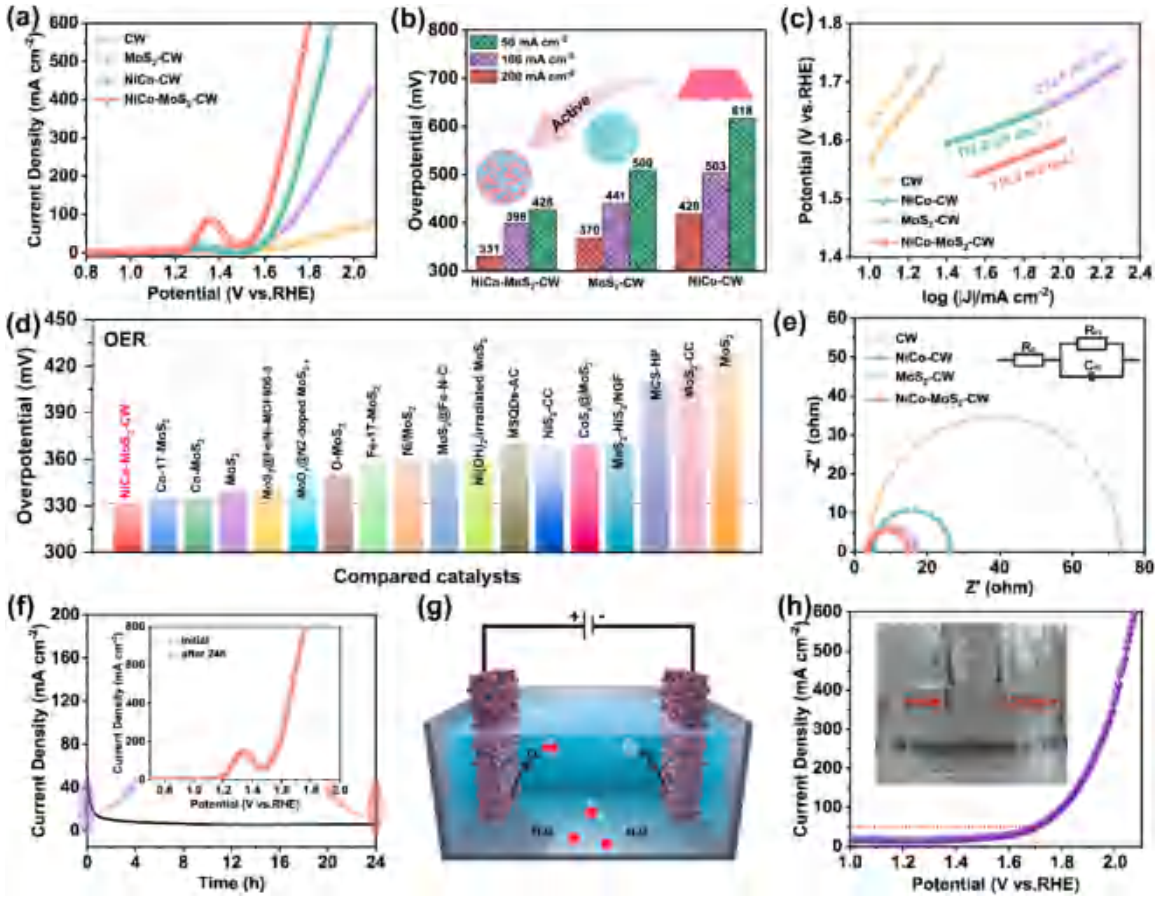

Fig. 5. OER performance of synthesized catalysts in 1.0 M KOH, a) the linear sweep voltammetry (LSV) curves of the CW, MoS_2-CW, NiCo-CW and NiCo-MoS_2-CW; b) comparison of OER overpotentials at 50 mA cm^{-2}, 100 mA cm^{-2} and 200 mA cm^{-2} for NiCo-CW, MoS_2-CW and NiCo-MoS_2-CW; c) Tafel slopes of the CW, NiCo-CW, MoS_2-CW and NiCo-MoS_2-CW; d) comparison of the OER performance of NiCo-MoS_2-CW with reported MoS_2-based catalysts at a current density of −10 mA cm^{-2}, originating from Table S4 (Supporting Information); e) Nyquist plots of the CW, NiCo-CW, MoS_2-CW and NiCo-MoS_2-CW; f) the chronoamperometry curve of NiCo-MoS_2-CW at the overpotential 150 mV, the inset shows LSV curves before and after 24 h; g) Schematic diagram of the overall water splitting system; h) LSV curves of the overall water splitting in a two-electrode system, the inset shows the bubbles of H_2 and O_2 generated from electrodes.

improvement in the rate of electron transfer after the modification with NiCo.

Fig. 5f shows a stability test at −150 mV (Vs. RHE) overpotential for 24 h. Excitingly, the almost constant current density throughout the test indicates that the NiCo-MoS_2-CW electrode has good durability. Simultaneously, it can be noted in Fig. 5f that the LSV curves demonstrate a significant resemblance before and after conducting the stability test, which serves as additional proof of the remarkable durability of NiCo-MoS_2-CW. In addition, the stability test did not result in noticeable alterations to the SEM image of the electrode surface when compared to its pre-test condition (Figure S12, Supporting Information), suggesting that the durability of the electrode's microstructure remained intact. At the same time, it can be observed (Figure S13 in the Supporting Information) that there were no changes in the XRD analysis results after conducting the stability test. This finding further provides the notion that the NiCo-MoS_2-CW electrode exhibits remarkable durability. Hence, based on these comprehensive tests, it can be concluded that the OER performance of the NiCo-MoS_2-CW electrode is exceptional.

3.4. Overall water splitting performance of NiCo-MoS_2-CW electrode

The NiCo-MoS_2-CW electrode demonstrates remarkable catalytic effectiveness in both the HER and OER. The electrode shown in Fig. 5g was employed as both the cathode and anode to construct a two-electrode electrolyzer. Subsequently, the overall water splitting performance were evaluated in a 1.0 M KOH solution. As depicted in Fig. 5h, the NiCo-MoS_2-CW || NiCo-MoS_2-CW electrolytic cell demonstrates remarkable electrocatalytic efficiency as a bifunctional electrode for overall water splitting, achieving a current density of 50 mA cm^{-2} with only 1.69 V cell voltage requirement. The water splitting process was documented using Fig. 5h for the digital photo and Movie 1 (Supporting Information) for the Movie of NiCo-MoS_2-CW bifunction electrodes. In addition, the stability of NiCo-MoS_2-CW as a bifunctional electrode for overall water splitting was demonstrated through the chronoamperometry curve presented in Figure S14 (Supporting Information). In particular, the negligible change in current observed over a 24 h at an electrolyzer pressure of 1.5 V highlights the exceptional durability performance of the bifunctional electrode.

4. Conclusions

The NiCo-modified 1T/2H MoS_2 onto carbonized wood (NiCo-MoS_2-CW) electrode was fabricated by in-situ loading of NiCo modified polyphase MoS_2 on CW using the hydrothermal method and electrodeposition method, exhibiting exceptional electrocatalytic performance for overall water splitting. The catalytic performance of the NiCo-MoS_2-CW electrode for both hydrogen evolution reaction and oxygen evolution reaction was significantly superior to that of the NiCo-CW and MoS_2-CW electrodes, indicating that NiCo modification adjusted the surface electronic structure, enhanced OH^- adsorption, and accelerated the Volmer step of the catalytic process. The XPS analysis and Tafel slope analysis revealed that the NiCo modification significantly enhanced the adsorption kinetics during catalysis. Therefore, the remarkable catalytic efficiency demonstrated by the NiCo-MoS_2-CW electrode in this study underscores the importance of modifying the electronic structure during electrode design.

CRediT authorship contribution statement

Mengliang Hu: Writing – review & editing, Writing – original draft, Visualization, Methodology, Investigation, Formal analysis, Data curation, Conceptualization. **Yuanpeng Qian:** Methodology. **Rumeng Zhang:** Investigation. **Chuigen Guo:** Project administration, Funding acquisition. **Lemin Yang:** Investigation. **Liping Li:** Project administration, Methodology, Funding acquisition.

Declaration of competing interest

The authors declare that they have no known competing financial interests or personal relationships that could have appeared to influence the work reported in this paper.

Data availability

Data will be made available on request.

Acknowledgements

This work was financially supported by the National Natural Science Foundation of China (32071694), College Students' Innovative Entrepreneurial Training Plan Program (202310564002), Guangzhou Science and Technology Project (201905010005). The authors also would like to thank Shiyanjia Lab (www.shiyanjia.com) for the TEM analysis.

Appendix A. Supplementary material

Supplementary data to this article can be found online at https://doi.org/10.1016/j.jcis.2024.07.209.

References

[1] J. Wang, H. Yang, F. Li, L. Li, J. Wu, S. Liu, T. Cheng, Y. Xu, Q. Shao, X. Huang, Sci. Adv. 8 (2022) eabl9271.
[2] M. Hu, Y. Qian, S. Yu, Q. Yang, Z. Wang, Y. Huang, L. Li, Small 20 (2024) 2305948.
[3] Q. Qin, H. Jang, P. Li, B. Yuan, X. Liu, J. Cho, Adv. Energy Mater. 9 (2019) 1803312.
[4] L. Cao, Q. Luo, J. Chen, L. Wang, Y. Lin, H. Wang, X. Liu, X. Shen, W. Zhang, W. Liu, Z. Qi, Z. Jiang, J. Yang, T. Yao, Nat. Commun. 10 (2019) 4849.
[5] S. Lee, I. Kim, H. Cho, C. Kim, Y. Lee, Appl. Catal. B-Environ. 284 (2021) 119729.
[6] Z. Huang, J. Song, Y. Du, S. Xi, S. Dou, J.M.V. Nsanzimana, C. Wang, Z.J. Xu, X. Wang, Nat. Energy 4 (2019) 329–338.
[7] M. Hu, Z. Wang, M. Li, C. Guo, L. Li, ACS Appl. Nano Mater. 5 (2022) 8175–8183.
[8] I.S. Amiinu, Z. Pu, X. Liu, K.A. Owusu, H.G.R. Monestel, F.O. Boakye, H. Zhang, S. Mu, Adv. Funct. Mater. 27 (2017) 1702300.
[9] G. Zhao, Y. Xing, Y. Liu, X. Wang, B. Zhang, W. Liao, X. Xu, Mater. Today Chem. 34 (2023) 101758.
[10] D. Zhang, H. Li, A. Riaz, A. Sharma, W. Liang, Y. Wang, H. Chen, K. Vora, Z.S. Di Yan, A. Tricoli, C. Zhao, F.J. Beck, K. Reuter, K. Catchpole, S. Karuturi, Energy Environ. Sci. 15 (2022) 185–195.
[11] Z. Wang, X. Zhou, H. Jin, D. Chen, J. Zhu, R. Hempelmann, L. Chen, S. Mu, J. Alloy. Compd. 908 (2022) 164565.
[12] D. Chen, J. Zhu, X. Mu, R. Cheng, W. Li, S. Liu, Z. Pu, C. Lin, S. Mu, Appl. Catal. B-Environ. 268 (2020) 118729.
[13] L. Huang, G. Wei, J. Wang, D. Li, S. Jia, S. Wu, T. Jiang, Y. Guo, Y. Liu, F. Ren, Adv. Energy Mater. 13 (2023) 2300651.
[14] L. Mu, S. Qiu, G. Zhao, B. Zhang, W. Liao, N. Zhao, X. Xu, J. Mater. Chem. A 12 (2024) 1714–1724.
[15] H. Jiang, L. Yan, S. Zhang, Y. Zhao, X. Yang, Y. Wang, J. Shen, X. Zhao, L. Wang, Nano-Micro Lett. 13 (2021) 215.
[16] H. Duan, C. Wang, G. Li, H. Tan, W. Hu, L. Cai, W. Liu, N. Li, Q. Ji, Y. Wang, Y. Lu, W. Yan, F. Hu, W. Zhang, Z. Sun, Z. Qi, L. Song, S. Wei, Angew. Chem. Int. Ed. Engl. 60 (2021) 7251–7258.
[17] D. Wang, X. Zhang, S. Bao, Z. Zhang, H. Fei, Z. Wu, J. Mater. Chem. A 5 (2017) 2681–2688.
[18] M. Hu, Z. Wang, M. Li, K. Pan, L. Li, Int. J. Hydrog. Energy 46 (2021) 28087–28097.
[19] X. Geng, W. Sun, W. Wu, B. Chen, A. Al-Hilo, M. Benamara, H. Zhu, F. Watanabe, J. Cui, T. Chen, Nat. Commun. 7 (2016) 10672.
[20] N. Zhang, C. Wang, F. Zhao, K. Han, Y. Ma, Y. Li, J. Liu, Appl. Catal. B-Environm. Energy 297 (2021) 120456.
[21] P. Man, S. Jiang, K.H. Leung, K.H. Lai, Z. Guang, H. Chen, L. Huang, T. Chen, S. Gao, Y. Peng, C. Lee, Q. Deng, J. Zhao, T.H. Ly, Adv. Mater. (2023) 2304808.
[22] F. Yang, R. Yao, Z. Lang, F. Yu, H. Dong, Y. Wang, Y. Li, H. Tan, ACS Energy Lett. 8 (2023) 5175–5183.
[23] L. Kong, C. Gao, Z. Liu, L. Pan, P. Yin, J. Lin, Chem. Eng. J. 479 (2024) 147725.
[24] G. Hai, X. Xue, Z. Wu, C. Zhang, X. Liu, X. Huang, J. Energy Chem. 91 (2024) 194–202.
[25] K. Nie, N. Li, B. Li, Y. Zhang, P. Liu, S. Chong, J. Hu, Z. Liu, W. Huang, Chem. Eng. J. 475 (2023) 146066.
[26] C. Wang, L. Yu, F. Yang, L. Feng, J. Energy Chem. 87 (2023) 144–152.
[27] I. Khan, Y. Chen, Z. Li, W. Liu, S. Khan, S. Ullah, L. Liu, A. Zada, S. Ali, S. Shaheen, L. Yang, J. Mater. Sci. Technol. 178 (2024) 210–225.
[28] B. Zhang, N. Zhang, G. Zhao, L. Mu, W. Liao, S. Qiu, X. Xu, J. Colloid. Interface. Sci. 665 (2024) 1054–1064.

[29] J. Kibsgaard, Z. Chen, B.N. Reinecke, T.F. Jaramillo, Nat. Mater. 11 (2012) 963–969.
[30] T. Ma, X. Shen, Q. Jiao, Y. Zhao, H. Li, Y. Zhang, Y. Lv, C. Feng, L. Guo, Chem. Eng. J. 464 (2023) 142592.
[31] Y. Tian, Y. Song, J. Liu, J. Ji, F. Wang, Chem. Eng. J. 398 (2020) 125554.
[32] Y. Sun, Y. Zang, W. Tian, X. Yu, J. Qi, L. Chen, X. Liu, H. Qiu, Energy Environ. Sci. 15 (2022) 1201–1210.
[33] H. Hou, H. Huo, Y. Yu, M. Li, Y. Chen, C. Chen, G. Qian, D. Min, Chem. Eng. J. 484 (2024) 149454.
[34] J. Bang, I.K. Moon, Y. Kim, J. Oh, Small Struct. 4 (2023) 2200283.
[35] M. Hu, Z. Wang, M. Li, C. Guo, L. Li, Int. J. Hydrog. Energy 48 (2023) 8819–8829.
[36] W. Gan, L. Wu, Y. Wang, H. Gao, L. Gao, S. Xiao, J. Liu, Y. Xie, T. Li, J. Li, Adv. Funct. Mater. 31 (2021) 2010951.
[37] Y. Qian, M. Hu, L. Li, S. Cao, J. Xu, J. Hong, X. Liu, J. Xu, C. Guo, Fuel 361 (2024) 130653.
[38] Y. Qian, M. Hu, L. Li, X. Liu, S. Cao, C. Guo, Int. J. Hydrog. Energy 48 (2023) 13543–13554.
[39] B. Zhang, J. Liu, J. Wang, Y. Ruan, X. Ji, K. Xu, C. Chen, H. Wan, L. Miao, J. Jiang, Nano Energy 37 (2017) 74–80.
[40] C. Zhang, Y. Xie, J. Liu, F. Cao, H. Cong, H. Li, Chem. Eng. J. 419 (2021) 129977.
[41] J. Hu, C. Zhang, L. Jiang, H. Lin, Y. An, D. Zhou, M.K.H. Leung, S. Yang, Joule 1 (2017) 383–393.
[42] J. Hu, C. Zhang, Y. Zhang, B. Yang, Q. Qi, M. Sun, F. Zi, M.K.H. Leung, B. Huang, Small 16 (2020) 2002212.
[43] J. Zhang, T. Wang, D. Pohl, B. Rellinghaus, R. Dong, S. Liu, X. Zhuang, X. Feng, Angew. Chem. Int. Ed. Engl. 55 (2016) 6702–6707.
[44] J.D. Wiensch, J. John, J.M. Velazquez, D.A. Torelli, A.P. Pieterick, M.T. Mcdowell, K. Sun, X. Zhao, B.S. Brunschwig, N.S. Lewis, ACS Energy Lett. 2 (2017) 2234–2238.
[45] K. Sun, L. Zeng, S. Liu, L. Zhao, H. Zhu, J. Zhao, Z. Liu, D. Cao, Y. Hou, Y. Liu, Y. Pan, C. Liu, Nano Energy 58 (2019) 862–869.
[46] K. Wang, K. Yu, S. Xu, S. Yuan, L. Xiang, B. Pang, J. Zheng, N. Li, Appl. Catal. B-Environ. 328 (2023) 122445.
[47] M. Liu, H. Chen, X. Tang, H. Liu, B. Tu, W. Guo, Y. Zheng, Y. Liu, Y. Tang, R. He, W. Zhu, Small 18 (2022) 2107444.
[48] M. Zheng, J. Du, B. Hou, C. Xu, ACS Appl. Mater. Interf. 9 (2017) 26066–26076.
[49] Q. Liu, Z. Xue, B. Jia, Q. Liu, K. Liu, Y. Lin, M. Liu, Y. Li, G. Li, Small 16 (2020) 2002482.
[50] Q. Xu, Y. Liu, H. Jiang, Y. Hu, H. Liu, C. Li, Adv. Energy Mater. 9 (2019) 1802553.
[51] R. Fan, J. Zhou, W. Xun, S. Cheng, S. Vanka, T. Cai, S. Ju, Z. Mi, M. Shen, Nano Energy 71 (2020) 104631.
[52] X. Zhang, Y. Liang, Adv. Sci. 5 (2018) 1700644.
[53] Y. Chen, X. Wang, M. Lao, K. Rui, X. Zheng, H. Yu, J. Ma, S.X. Dou, W. Sun, Nano Energy 64 (2019) 103918.
[54] Y. Qian, J. Yu, Z. Lyu, Q. Zhang, T.H. Lee, H. Pang, D.J. Kang, Carbon Energy (2023) e376.
[55] Y. Yang, H. Yao, Z. Yu, S.M. Islam, H. He, M. Yuan, Y. Yue, K. Xu, W. Hao, G. Sun, H. Li, S. Ma, P. Zapol, M.G. Kanatzidis, J. Am. Chem. Soc. 141 (2019) 10417–10430.
[56] Y. Yang, K. Zhang, H. Ling, X. Li, H.C. Chan, L. Yang, Q. Gao, ACS Catal. 7 (2017) 2357–2366.
[57] Z. Sun, L. Lin, M. Yuan, H. Yao, Y. Deng, B. Huang, H. Li, G. Sun, J. Zhu, Nano Energy 101 (2022) 107563.
[58] Z. Zhu, H. Yin, C. He, M. Al-Mamun, P. Liu, L. Jiang, Y. Zhao, Y. Wang, H. Yang, Z. Tang, D. Wang, X. Chen, H. Zhao, Adv. Mater. 30 (2018) 1801171.
[59] B. Mohanty, M. Ghorbani-Asl, S. Kretschmer, A. Ghosh, P. Guha, S.K. Panda, B. Jena, A.V. Krasheninnikov, B.K. Jena, ACS Catal. 8 (2018) 1683–1689.
[60] C. Qin, A. Fan, X. Zhang, S. Wang, X. Yuan, X. Dai, J. Mater. Chem. A 7 (2019) 27594–27602.
[61] C. Wang, L. Zhang, G. Xu, L. Yang, J. Yang, Chem. Eng. J. 417 (2021) 129270.
[62] F. Gong, S. Ye, M. Liu, J. Zhang, L. Gong, G. Zeng, E. Meng, P. Su, K. Xie, Y. Zhang, J. Liu, Nano Energy 78 (2020) 105284.
[63] G. Wang, G. Zhang, X. Ke, X. Chen, X. Chen, Y. Wang, G. Huang, J. Dong, S. Chu, M. Sui, Small 18 (2022) 2107238.
[64] P. Kuang, M. He, H. Zou, J. Yu, K. Fan, Appl. Catal. B-Environ. 254 (2019) 15–25.
[65] X. Lei, K. Yu, H. Li, Z. Zhu, Electrochim. Acta 269 (2018) 262–273.
[66] X. Mu, Y. Zhu, X. Gu, S. Dai, Q. Mao, L. Bao, W. Li, S. Liu, J. Bao, S. Mu, J. Energy Chem. 62 (2021) 546–551.
[67] Y. Liu, S. Jiang, S. Li, L. Zhou, Z. Li, J. Li, M. Shao, Appl. Catal. B-Environ. 247 (2019) 107–114.
[68] Y. Qian, J. Yu, Y. Zhang, F. Zhang, Y. Kang, C. Su, H. Shi, D.J. Kang, H. Pang, Small Methods 6 (2022) 2101186.
[69] Y. Wang, S. Liu, X. Hao, S. Luan, H. You, J. Zhou, D. Song, D. Wang, H. Li, F. Gao, J. Mater. Chem. A 7 (2019) 10572–10580.
[70] Y. Wang, Y. Zhou, M. Han, Y. Xi, H. You, X. Hao, Z. Li, J. Zhou, D. Song, D. Wang, F. Gao, Small 15 (2019) 1805435.
[71] Y. Yan, S. Liang, X. Wang, M. Zhang, S. Hao, X. Cui, Z. Li, Z. Lin, Proc. Natl. Acad. Sci. U. S. A. 118 (2021) e2110036118.
[72] Z. He, Q. Liu, Y. Zhu, T. Tan, L. Cao, S. Zhao, Y. Chen, ACS Appl. Energ. Mater. 3 (2020) 7039–7047.
[73] Z. Lin, T. Feng, X. Ma, G. Liu, Fuel 339 (2023) 127395.